Supplementary Information: Shape curvature effects in viscous streaming

Yashraj Bhosale[1], Tejaswin Parthasarathy[1], and Mattia Gazzola[1,2]†

[1]Mechanical Sciences and Engineering, University of Illinois at Urbana-Champaign, Urbana, IL 61801, USA

[2]National Center for Supercomputing Applications, University of Illinois at Urbana-Champaign, Urbana, IL 61801, USA

(Received xx; revised xx; accepted xx)

1. Curvature variation setup: cylinders in an infinite regular lattice

Here we provide further details relative to our setup, which consists of a lattice of cylinders with two discrete curvatures. With a computational domain of range $[0, 1]$, we instantiate a lattice of 16 cylinders in a 4×4 grid with periodic boundary conditions. To accommodate 4 cylinders in our domain, while allowing a curvature variation up to $\kappa_{\max}/\kappa_{\min} = 6$, we fix $\kappa_{\max} = 0.02$ as a reference length scale. Then the constant centre-to-centre distance between these cylinders is $s = 1/4 = 0.25 = 12.5\kappa_{\max}$. Maintaining s constant allows us to consistently compare systems characterized by different curvature ratios. The value of s is chosen to span a reasonable curvature ratio range, and at the same time is practical from an experimental, fabrication standpoint. The oscillatory amplitude (A) for all the cylinders in the lattice is kept constant ($A\kappa_{\max} = 0.1$). This is because oscillating the fluid with constant amplitude is experimentally convenient. By virtue of keeping a constant amplitude, the streaming flow for the lattice system can be characterized with one value of R_s ($R_s = A^2\omega/\nu$). Lastly, fixing a constant amplitude allows us to extend our understanding (with two curvatures) to individual complex shapes with multiple curvatures. Indeed all local curvatures of an individual streaming body undergo the same absolute oscillation amplitudes. We not here that we performed cursory phase space explorations for different spacings between cylinders, and observed that the qualitative nature of the emerging streaming fields is preserved, although the boundaries between different topological phases shift quantitatively.

2. Lattice system: flow bifurcations

2.1. *Heteroclinic orbit bifurcation via asymmetric background flow*

Here we revisit the heteroclinic orbit bifurcation observed for the transition II $\rightarrow$ V of figure 4 in the main text. We identified the reduced Hamiltonian form with the unfolding term coefficient β that represents symmetry ($\beta = 0$) or asymmetry ($\beta \neq 0$) in our lattice setup (figure 1(*a, b*)). We now demonstrate that the notion of breaking symmetry extends to more than just curvature variation, by breaking symmetry via the superposition of a uniform background flow. Figure 1(*c*) presents a Phase II flow topology. We focus on the highlighted saddles and the heteroclinic orbits joining them. As we break symmetry along the horizontal axis by imposing a slow mean flow, we observe the predicted flow topology change (figure 1(*d*)), where the vertically oriented heteroclinic orbits break up, while the

† Email address for correspondence: mgazzola@illinois.edu

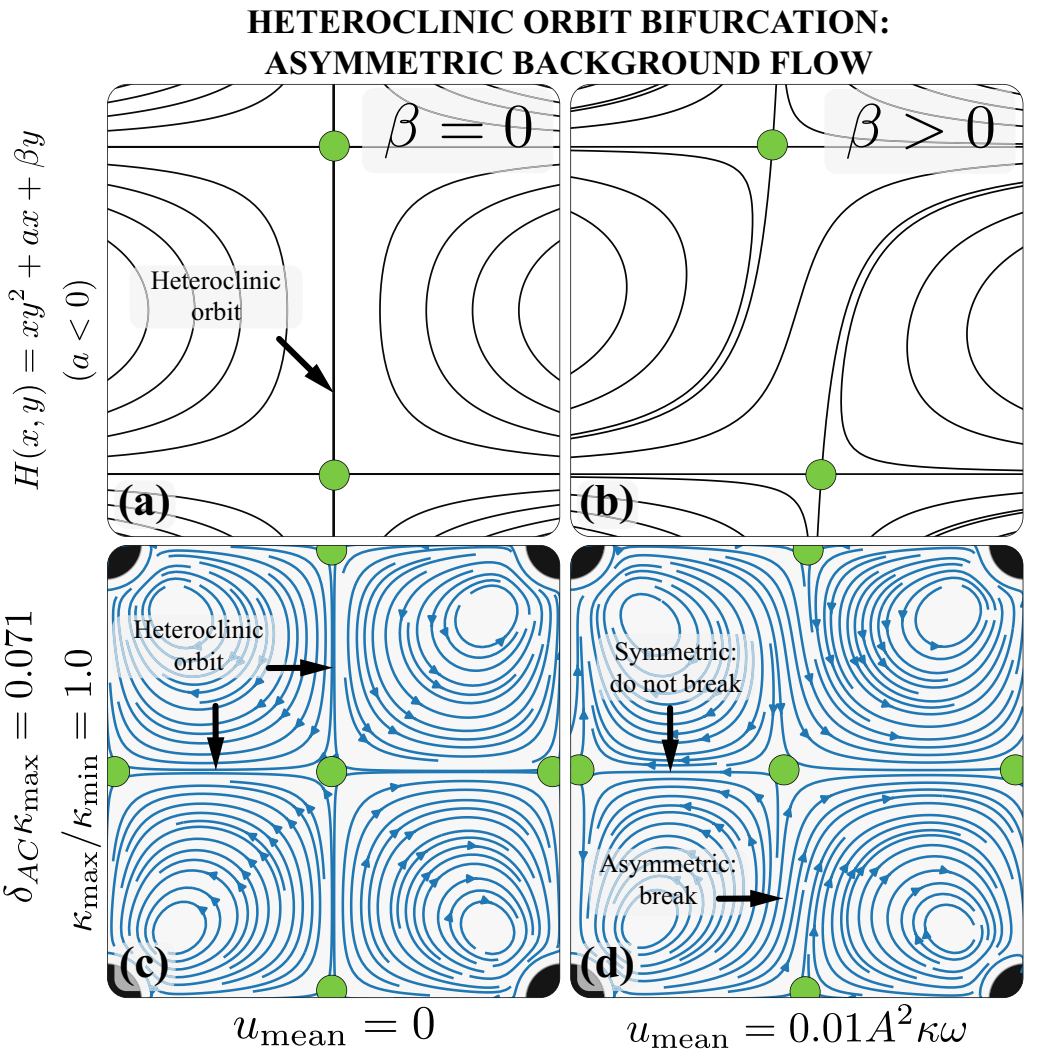

FIGURE 1. Asymmetric background flow. We demonstrate that the heteroclinic orbit bifurcation, associated with the transition II $\rightarrow$ V in the lattice phase space, can be triggered by breaking symmetry via superimposing a slow uniform background flow, instead of using curvature variations as in the main text. (*a, b*) present the reduced Hamiltonian form for the bifurcation, with the flow topology change on imposing the mean flow in the lattice system, shown in (*c, d*). We note that in (*c, d*) all cylinders present the same radius so that $\kappa_{\max}/\kappa_{\min} = 1$.

horizontally oriented ones do not. Through this illustration, we demonstrate that the control on asymmetry via means other than curvature variation leads to identical flow topology rearrangements. This confirms the physical intuiton provided by the identified reduced Hamiltonian form.

2.2. *Reflecting umbilic bifurcation: two step rationale*

We now focus on the transition between Phase VI and VII in the lattice phase space. We notice that the system appears symmetric about the horizontal and vertical axes. Yet, the transition into Phase VII occurs in two distinct steps: 1) a hyperbolic reflecting umbilic bifurcation that involves a topological rearrangement about the vertical axis of symmetry

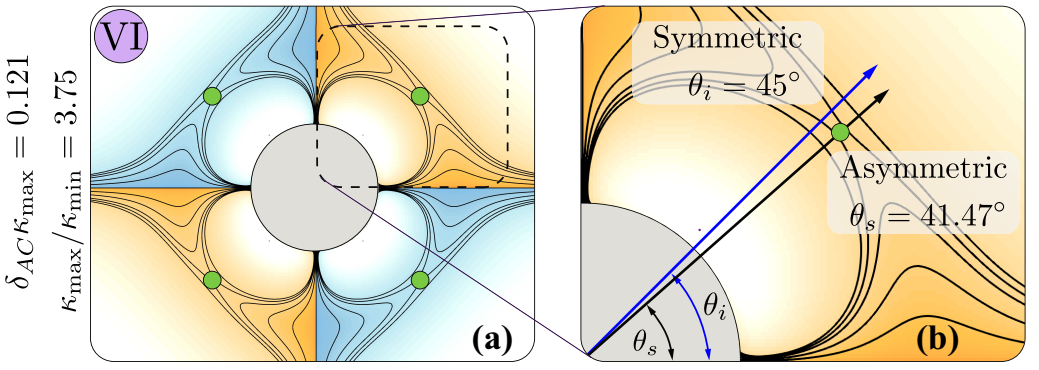

FIGURE 2. Reflecting umbilic bifurcation. (a) Illustration of the flow topology near the smaller cylinder for Phase VI. (b) Angular location of the highlighted saddle observed in simulations θ_s, compared to the expected symmetric location θ_i. This small yet non-negligible difference creates asymmetry between the flow topology along the vertical and horizontal axes, resulting in the two step reflecting umbilic bifurcation.

of the cylinder, and 2) an elliptic reflecting umbilic bifurcation that involves a topological rearrangement about the horizontal axis of symmetry of the cylinder. To investigate this preference for one axis over another, we focus on figure 2(a), which depicts the flow topology near the smaller cylinder in Phase VI. We focus on the highlighted saddles and the corresponding local flow topology depicted in figure 2(b). We notice a small yet non-negligible difference between the angular location of the highlighted saddle in simulations (θ_s), and the expected location (θ_i) based on the symmetry of the setup. Upon increasing simulation's resolution, or varying background flow oscillation direction, the magnitude of this angular deviation can be reduced, but not removed, so that a small preference persists. We attribute this small preferential deviation to the fact that the cylinders location is not (and cannot be) perfectly aligned with the discretization grid.

This small local deviation from symmetry is responsible for the observed sequence of umbilic bifurcations. The sequence order is found to be robust: indeed a saddle misalignment with respect to the 45° angle consistently triggers the hyperbolic reflecting umbilic bifurcation first (as $\delta_{AC}\kappa$ decreases), either on the vertical or horizontal axis, depending on $\theta_s < 45°$ or $\theta_s > 45°$. The induced local topological rearrangement is then found to be the natural precursor of the elliptic reflecting umbilic bifurcation, which occurs on the axis perpendicular to the first bifurcation. Therefore, to summarize, the boundaries between Phase VI, hidden Phase H and Phase VII are robustly associated with the bifurcation identified in the main text, as empirically verified though the comparison with triangle and square experiments. We note that in a perfect lattice, this series of two steps may coalesce in a single step. Nonetheless, this is only a theoretical scenario which we could not attain computationally and that cannot be expected to manifest experimentally.

2.3. *Phase I → II: higher order reflecting umbilic bifurcation*

Here, we illustrate the bifurcation Phase I → II, as depicted in figure 3(a). To identify this bifurcation we focus on two adjacent unit cell quadrants of the lattice. We note the absence of driven flow regions around the cylinders in Phase I (figure 3(b)) and their presence in phase II (figure 3(k), marked in pink). This flow topology change occurs in two consecutive steps, passing through another hidden phase of §4.2.8 in the main text.

In the first step, we draw attention to the absence of recirculating regions in Phase I (figure 3(b)) and their presence in figure 3(d) (comprised of five saddles and four centres,

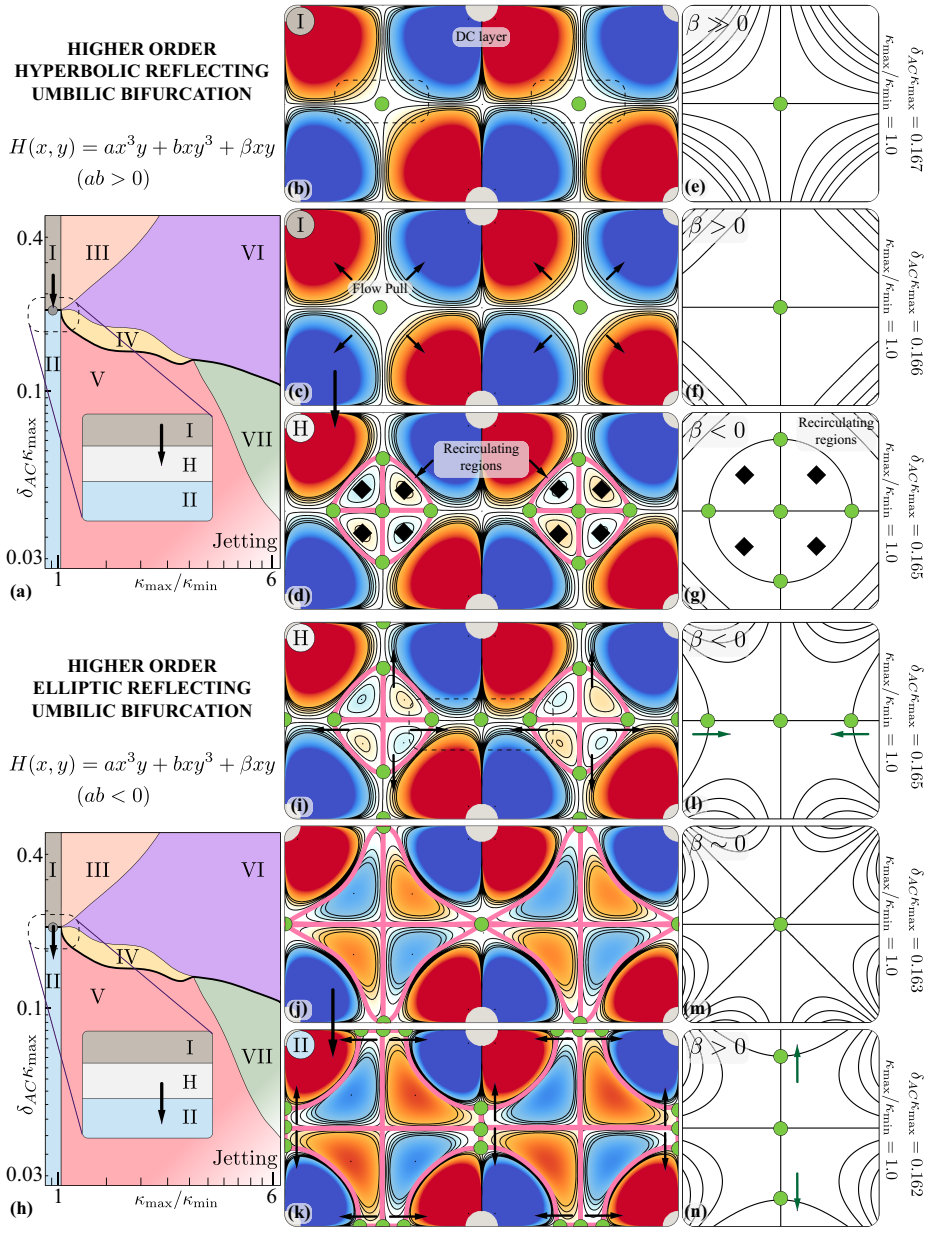

FIGURE 3. Phase I → hidden Phase H: higher order hyperbolic reflecting umbilic bifurcation. (*a*) The transition is highlighted on the phase space (with a zoomed in view) and the corresponding reduced Hamiltonian form is reported. (*b, c, d*) Flows representative of Phase I, Phase I approaching the transition, and hidden Phase H, respectively. (*e, f, g*) Bifurcations captured as contours of the reduced Hamiltonian form. (*h*) The transition from hidden Phase H → II (higher order elliptic reflecting umbilic bifurcation) is highlighted on the phase space (with a zoomed in view) and the corresponding reduced Hamiltonian form is reported. (*i, j, k*) Flows representative of hidden Phase H, at the transition, and Phase II, respectively. (*l, m, n*) Bifurcations captured as contours of the reduced Hamiltonian form. The newly created recirculating region pairs are marked in pink.

marked in pink). We note that the latter flow field corresponds to the hidden Phase H. The simplest Hamiltonian form that captures this transition is $H(x,y) = ax^3y + bxy^3 + \beta xy$ with $ab > 0$, which corresponds to a higher order hyperbolic reflecting umbilic bifurcation (higher order with respect to the ones shown in the main text, on account of the additional symmetry due to same curvature cylinders) (Bosschaert & Hanßmann 2013). Here βxy is the unfolding term, that controls the appearance (going from $\beta > 0$ to $\beta < 0$) of the recirculating regions and their size (figure 3(*e-g*)). In our lattice system, the appearance and size of these regions can be controlled by decreasing δ_{AC}, which decreases the DC layer thickness δ_{DC} of all the cylinders. This pulls the streamlines adjacent to the marked saddle, in four opposite directions (figure 3(*c*)), causing it to eventually split into five saddles and four centres (figure 3(*d*)). Topologically, this manifests as four counter-rotating recirculating regions, thus revealing Phase H.

The second step of the Phase I $\rightarrow$ II transition occurs upon further decreasing δ_{AC}, immediately after the previous bifurcation, thus rendering the hidden Phase H very narrow. We focus on the saddles in the highlighted region of the unit cell, in the hidden Phase H (figure 3(*i*)). After the transition these saddles are located on the vertical axis passing through the highlighted region, thus recovering Phase VII (figure 3(*k*)). The simplest Hamiltonian form that captures this rearrangement is $H(x,y) = ax^3y + bxy^3 + \beta xy$ with $ab < 0$, which corresponds to a higher order elliptic reflecting umbilic bifurcation (Bosschaert & Hanßmann 2013). Here βxy is the unfolding term, that captures whether the saddles are present ($\beta < 0$) or absent ($\beta > 0$) on the horizontal axis (figure 3(*l-n*)), as well as their distance. Similar to the previous step, a decrease in δ_{AC} (i.e $\delta_{DC} \downarrow$) causes a pull on the streamlines immediately adjacent to the cylinder's DC layers. This time though, the saddles created in the previous step are now pushed towards the saddle on the vertical axis in the highlighted region, extending the recirculating region pairs. Upon reaching the saddle on the vertical axis, the two opposite saddles collapse (figure 3(*j*)) and split along the vertical axis (figure 3(*k*)). We note that this bifurcation is observed along all the edges of the unit cell. These new saddles completely define the driven flow regions around the cylinders, thus recovering Phase II.

3. Effects of lattice spacing variation on the phase space

Here we illustrate the effects of varying centre-to-centre spacing s between the cylinders, on the lattice system phase space. Figure 4 presents three different lattice phase spaces with three different spacings ($s\kappa_{\max} = 6.25, 12.5$ (main text) and 25). Inaccessible regions of curvature (due to unphysical cylinder–cylinder surface overlap) are marked in grey. First, we observe no additional flow bifurcations/phases in the system as spacing is varied, confirming the qualitative picture provided in the main text. Second, as the spacing increases the phase boundaries corresponding to the supercritical pitchfork bifurcation (Phases IV $\rightarrow$ VI and V $\rightarrow$ VII), which result due to the interaction between the driven flow regions of the larger cylinders, are pushed towards high $\kappa_{\max}/\kappa_{\min}$ regions. We predict that eventually at sufficiently large spacing, these boundaries and corresponding phases will vanish, thus reducing the richness of the system. Third, in the limit of large spacing ($s\kappa_{\max} \rightarrow \infty$, i.e. in an unbounded domain) the interaction between cylinders becomes less and less important, so that practically only Phases I and II will be retained (figure 1 of main text). This is intuitively consistent since this scenario effectively correspond to individual cylinders in an unbounded domain, for which only single and double boundary layer regimes are possible.

We further rationalize our results by presenting the streaming-velocity decay fields for varying lattice spacings. Figure 5(*a*) presents the velocity profiles along the horizontal

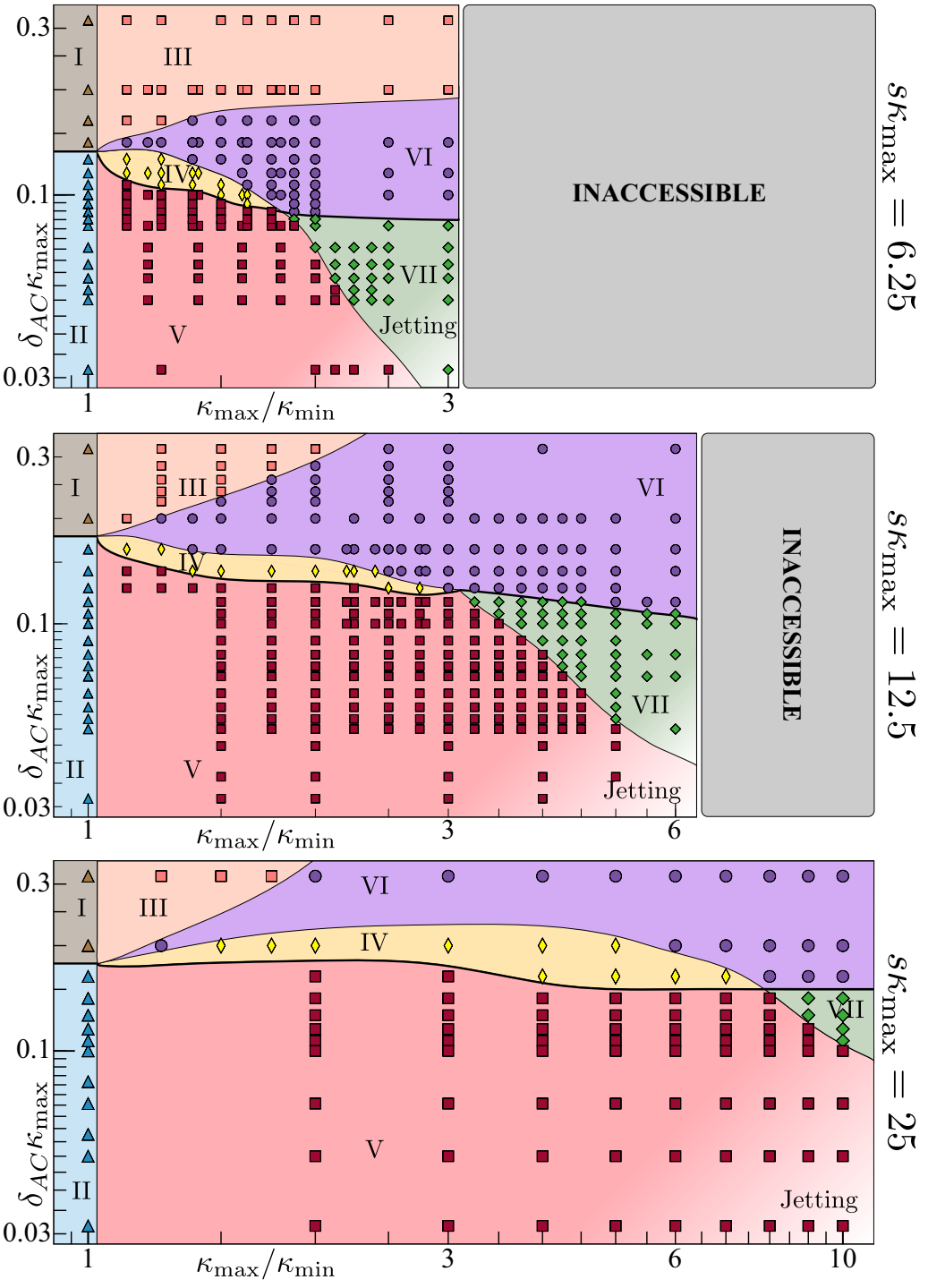

FIGURE 4. Effects of lattice spacing variation: Three different lattice phase spaces with varying cylinder separation distances $s\kappa_{\max}$ are shown to demonstrate its effect on the phase boundaries. Inaccessible regions (due to cylinder–cylinder surface overlap) are marked in grey.

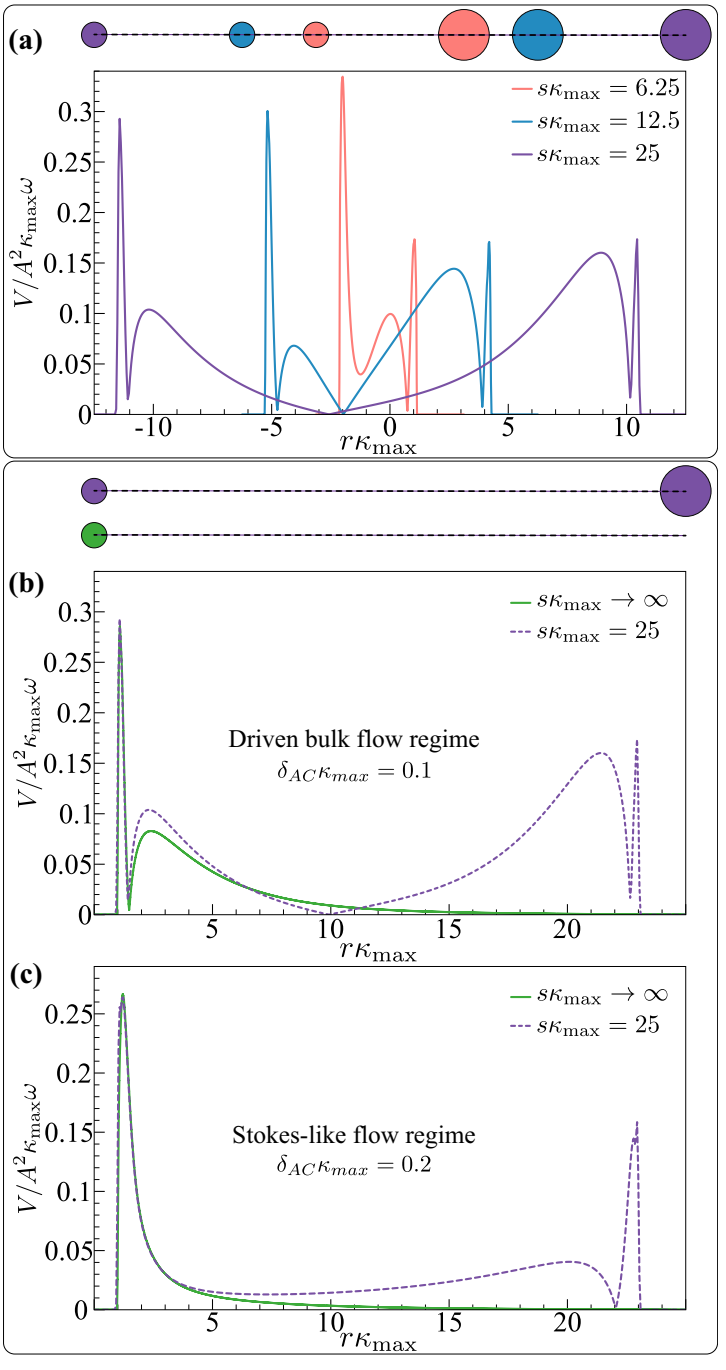

FIGURE 5. Effects of lattice spacing variation: (a) Non-dimensional velocity magnitude profiles along the horizontal axis passing through centers of cylinders of two different radii ($\kappa_{\max}/\kappa_{\min} = 2$), as a function of the distance from the point equidistant from the cylinder centers, for three different center-to-center spacings in the lattice. Comparison between velocity magnitude profile for the smaller cylinder in the lattice with the largest spacing ($s\kappa_{\max} = 25$) compared to the velocity magnitude profile for a single cylinder with the same $\delta_{AC}\kappa$ in an unbounded domain in (b) driven bulk flow regime and (c) Stokes-like flow regime.

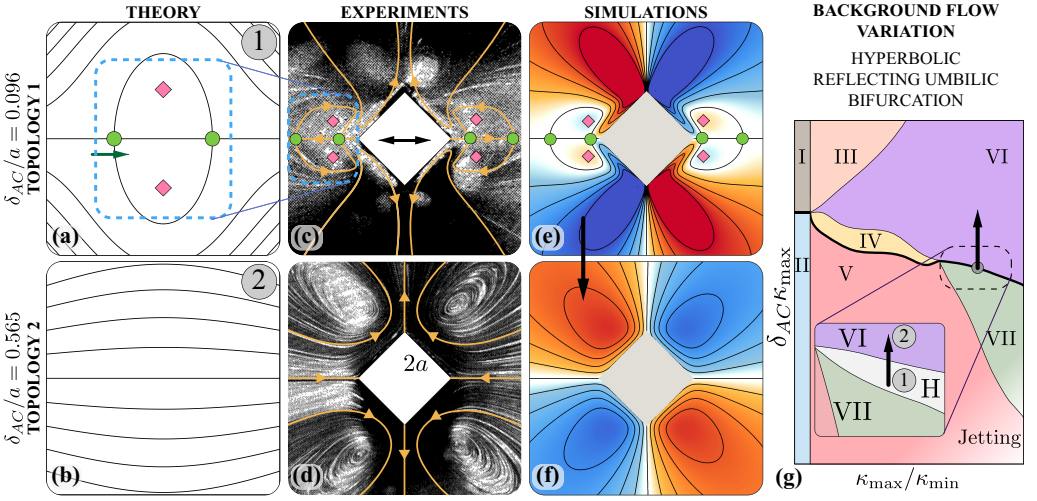

FIGURE 6. Background flow variation for a diamond cylinder. (*a, b*) Reduced Hamiltonian form contours for hyperbolic reflecting umbilic bifurcation, associated with the transition hidden Phase H → Phase VI in the lattice phase space. A topologically equivalent transition is observed on increasing δ_{AC}/a, both in experiments (*c, d*) and simulations (*e, f*). (*g*) Mapping of the observed transition on the lattice phase space.

axis passing through the centers of cylinders of two different radii ($\kappa_{max}/\kappa_{min} = 2$), for different spacings, such that the equidistant point is always situated on the origin ($r\kappa_{max} = 0$). Here, the smaller cylinder is to the left of the origin, while the larger cylinder is to the right. As the lattice spacing increases, the velocity profiles change qualitatively and eventually approach the unbounded single cylinder limit. This is shown for the smaller cylinder in figure 5(*b*), where the velocity profile for the highest spacing case ($s\kappa_{max} = 25$, dashed purple) is overlaid with an equivalent profile for a single cylinder oscillating in the driven-bulk flow regime (in green). This equivalence is also noticed in the Stokes-like flow regime, which we show in figure 5(*c*).

We conclude based on both these observations that as the lattice spacing increases, the streaming flows generated due to individual cylinders effectively interact to a lesser extent. This in turn reduces the range of different flow topologies/bifurcations that can be observed, to the ones that simply correspond to superposition of their individual streaming flow fields, in the limit of high spacing.

4. Generalization to individual streaming bodies: additional examples

Here we provide a number of additional examples which demonstrate that our intuition from the phase space carries on to various streaming geometries and oscillatory background flow conditions. All subsequent studies entail a single shape immersed in an unbounded domain.

4.1. *Comparison against experiments: streaming triangles and diamonds*

Expanding on the examples of the main text, we further test our understanding against a different set of experiments. We consider an oscillating diamond cylinder (of side $2a$) (Tatsuno 1974) and a horizontally oriented triangle cylinder (of side $2a$) (Tatsuno 1975).

Figure 6 illustrates the hyperbolic reflecting umbilic bifurcation for a diamond cylinder, observed on increasing δ_{AC}/a from 0.096 to 0.565, similar to the one observed in the

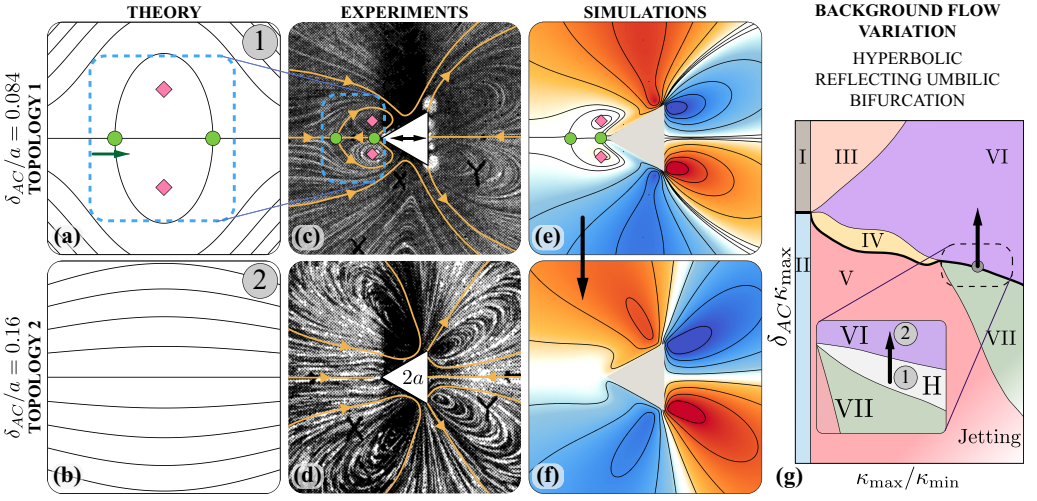

FIGURE 7. Background flow variation for a horizontally oriented equilateral triangle cylinder. (*a, b*) Reduced Hamiltonian form contours for hyperbolic reflecting umbilic bifurcation, associated with the transition hidden Phase H → Phase VI in the lattice phase space. A topologically equivalent transition is observed on increasing δ_{AC}/a, both in experiments (*c, d*) and simulations (*e, f*). (*g*) Mapping of the observed transition on the lattice phase space.

lattice phase space. Figure 6(*a, b*) illustrates the predicted flow topology change based on the reduced Hamiltonian contours, with confirmations against flow topologies observed in experiments (figure 6(*c, d*)) and simulations (figure 6(*e, f*)).

Figure 7 illustrates the hyperbolic reflecting umbilic bifurcation for the triangle cylinder, observed on increasing δ_{AC}/a from 0.084 to 0.16, similar to the one observed in the lattice phase space. Once again experiments (figure 7(*c, d*)) and simulations (figure 7(*e, f*)) confirm our predictions.

4.2. *Shape parametrization*

Figure 8 illustrates the parameterization for the complex convex shapes, investigated in §5.2 of the main text and in §4.3 of the supplementary information. Figure 8(*a*) presents the parametrization for the hybrid circular–square bullet of figure 12(*a*) in the main text. This hybrid cylinder presents top-down asymmetry—the top side is a circle with constant curvature κ_0, while the bottom is a square with rounded corners of constant curvature κ_v. As κ_v is varied from κ_0 to higher values ($\to \infty$), the shape morphs from a circle to a circle–square hybrid with increasingly sharper corners. Figure 8(*b*) presents the parametrization for the hybrid circular–elliptic cylinder, which we use to demonstrate additional examples of flow topology design in the following sections. This hybrid cylinder presents left-right asymmetry— the right side is a circle with constant curvature κ_0, while the left side is an ellipse of aspect ratio AR (defined as height/breadth, where height is kept constant). As AR is varied from 1 to higher values, the shape morphs from a circle to a circular–elliptic cylinder with a higher AR elliptic side (with corresponding higher curvature at the corners).

4.3. *Manipulation of streaming flow topology: circle to a circle–ellipse*

Figure 9(*a*) illustrates the morphing from a circular cylinder of uniform aspect ratio (AR = 1, defined as height/breadth) to a body with a circular side having the same curvature κ_0 and an elliptic side with aspect ratio AR > 1. Parametrization of this

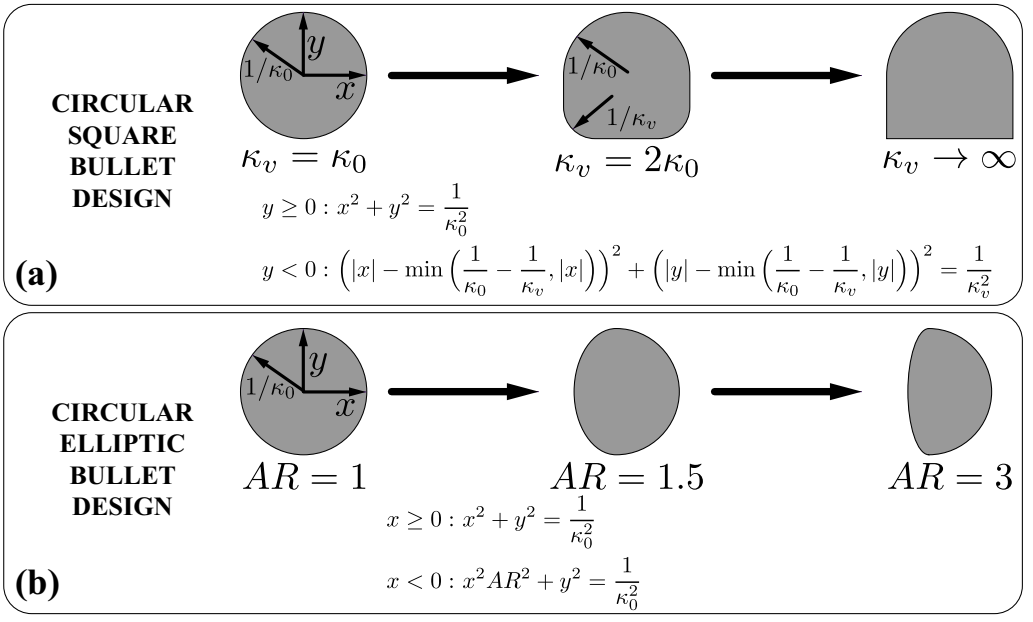

FIGURE 8. Parametrization of (a) the hybrid circular–square cylinder (main text) and (b) the circular–elliptic cylinder.

hybrid shape can be found in figure 8(b). For such AR, the body presents constant curvature κ_0 on the circular side and a range of curvatures (κ_0/AR to AR$^2\kappa_0$) on the elliptic side, thus introducing curvature variation in a regulated fashion.

We start by choosing a $\delta_{AC}\kappa_{\max}$ for which the streaming flow topology for a circular cylinder (AR = 1) lies in the finite thickness DC layer regime (figure 9(d)). We focus on the heteroclinic orbits highlighted in figure 9(d). Recalling our observations from the lattice system, we predict that introducing fore-aft shape asymmetry will lead to the breaking of these orbits, as captured by the heteroclinic orbit bifurcation from Phase II $\to$ V (figure 9(b, c)) in the main text. Indeed, testing a shape with curvature asymmetry (i.e. AR $>$ 1) confirms this prediction, as seen from the flow topology in figure 9(e).

After testing our understanding against the effects of breaking symmetry, we analyse how flow topology evolves on further increase in curvature variation (i.e. increase in AR) for the body. Figure 10(e) depicts the streaming flow topology for the body with AR $>$ 1, where the shape parameters and flow topology are retained from figure 9(e). We focus on the highlighted saddle (defining DC layer extent) forming the homoclinic orbit, and the centre within this orbit. As AR increases, (figure 10(a)), the local curvature on the body near the saddle increases. Based on the transitions V $\to$ VII and III $\to$ VI associated with such a curvature increase in the lattice phase space, we predict that this will lead to a decrease in the saddle–centre distance, while shrinking the corresponding homoclinic orbit. Then beyond a critical value of AR the orbit will eventually disappear through a saddle–centre annihilation, similar to the bifurcation seen from Phase V $\to$ VII. Figure 10(b, c, d) demonstrate the reduced Hamiltonian form contours for this system and showcase the saddle–centre bifurcation. Indeed, testing a shape with curvature variation (higher AR) confirms these predictions, as seen from the flow topologies in figure 10(f, g).

For completion, figure 11 presents a step-by-step systematic variation of geometric and background flow properties for the morphing from a circular cylinder to a hybrid circular–

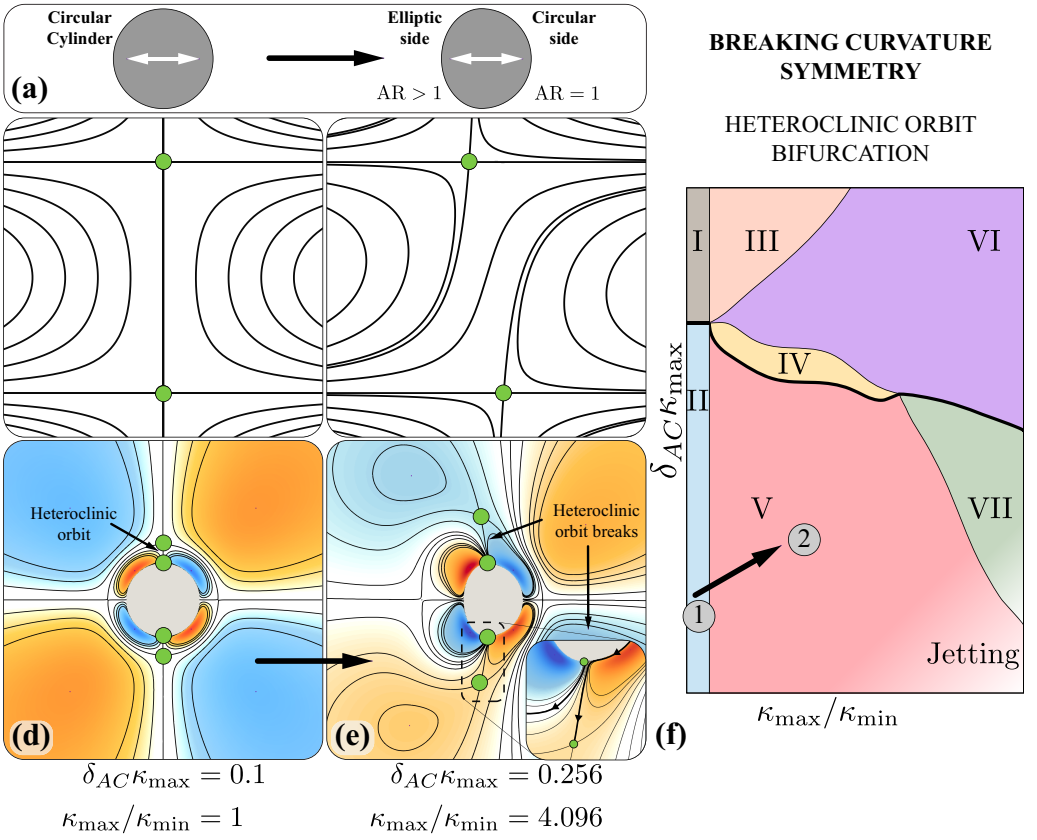

FIGURE 9. Breaking symmetry. (*a*) Illustration of morphing a circular cylinder into a hybrid circular–elliptic cylinder with a circular side and an elliptic side with varying aspect ratio (AR). (*b, c*) present the reduced Hamiltonian form contours for heteroclinic orbit bifurcation, associated with the transition II → V in the lattice phase space. The morphed body presents a topologically equivalent transition on breaking symmetry, presented in (*d, e*). (*f*) Mapping of the observed transition on the lattice phase space.

elliptic cylinder. We observe a wide range of flow topologies, which are predicted (reduced Hamiltonian as grey contours) by drawing intuition from the transitions observed in the lattice phase space with corresponding confirmations from simulations. We note that the same set of bifurcations as that of the circular–square cylinder in the main text, are encountered for the circular–elliptic cylinder. Figure 11(*b, c*) illustrate the heteroclinic orbit bifurcation (prediction and confirmation), observed on breaking symmetry described above. Figure 11(*c, d*) illustrate the saddle–centre bifurcation (prediction and confirmation), observed on curvature variation described above. Figure 11(*d, e*) and figure 11(*e, f*) illustrate the elliptic reflecting umbilic bifurcation and the hyperbolic reflecting umbilic bifurcation, respectively, observed on increasing δ_{AC} in the lattice phase space, with the predicted flow topology change based on the reduced Hamiltonian contours and confirmations against flow topologies observed in simulations.

In summary, this section illustrates an additional example of how our approach can be employed to predict and design streaming flow topologies, in a rational fashion.

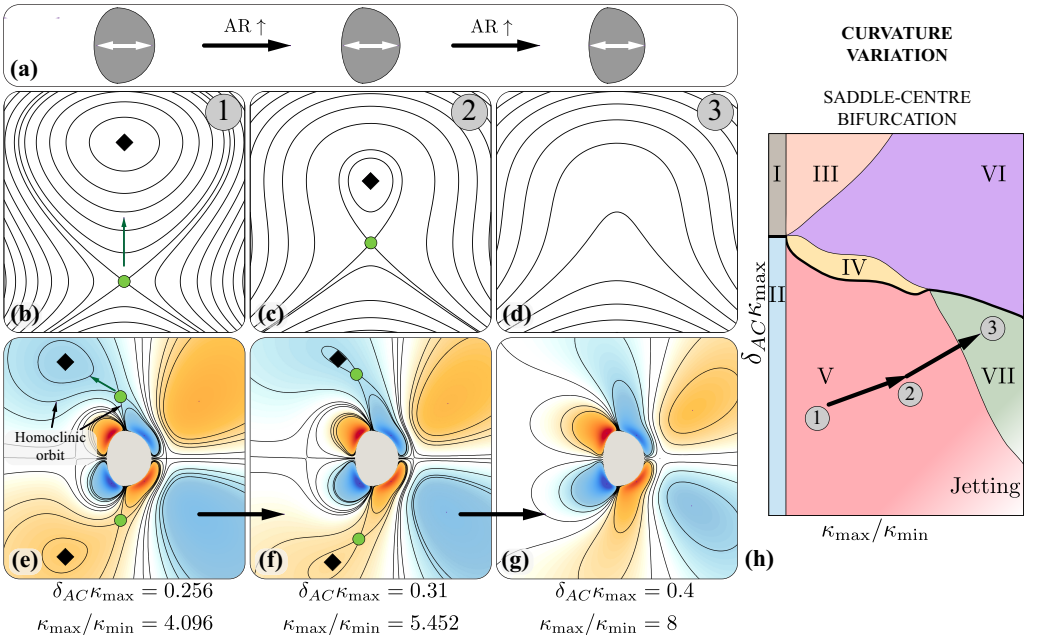

FIGURE 10. Varying curvature ratio. (a) Illustration of increasing curvature variation (increasing AR) for the circular–elliptic hybrid. (b, c, d) present the reduced Hamiltonian form contours for saddle–centre bifurcation, similar to the supercritical pitchfork bifurcation, associated with the transition V $\rightarrow$ VII in the lattice phase space. A topologically equivalent transition is observed on morphing the body, presented in (e, f, g). (h) Mapping of the observed transition on the lattice phase space.

4.4. *Varying ellipse aspect ratio*

Figure 12(a) illustrates the use of our phase space in the case of ellipses of varying aspect ratio (defined as height/breadth). We keep the major axis (height = L) fixed. This allows us to introduce curvature variation in a regulated fashion by spanning AR. We start by choosing a $\delta_{AC}\kappa_{\max}$ and AR for which the streaming flow topology for the ellipse lies in the finite thickness DC layer regime (figure 12(b)). We note that a mapping of this local flow topology to Phase I and II of our lattice system is not possible due to the variation of curvature on an ellipse (Phase I and II necessitate constant curvature). Additionally, mapping to Phases III, IV and V does not exist as we do not break fore-aft or top-down shape symmetry when we vary AR for an ellispe (figure 12(a)). This means that we don't break symmetry for the DC layer bounding heteroclinic orbits which are necessary for Phases III, IV and V to exist.

We focus on the highlighted saddles bounding the DC layers on the vertical axis, near the top and bottom ends of the ellipse. These structures closely resemble Phase VII of figure 7(k, n) in the main text, where the second saddle (not imaged in experiments) is located at infinity. Thus, as $\delta_{AC}\kappa_{\max}$ increases (on increasing AR), we predict that the saddles will progressively move outwards, to approach the saddles at infinity and undergo an elliptic reflecting umbilic bifurcation. This has the overall effect to "open up" the DC layers on the vertical axis of the ellipse. Additionally, we note that the highlighted flow structures on the left/right of the streaming shape can be mapped to Phase H of figure 7(d, g) (with one saddle at infinity). Therefore, as a side effect of the increase in $\delta_{AC}\kappa_{\max}$, we predict that the saddles at infinity enter the imaged domain and

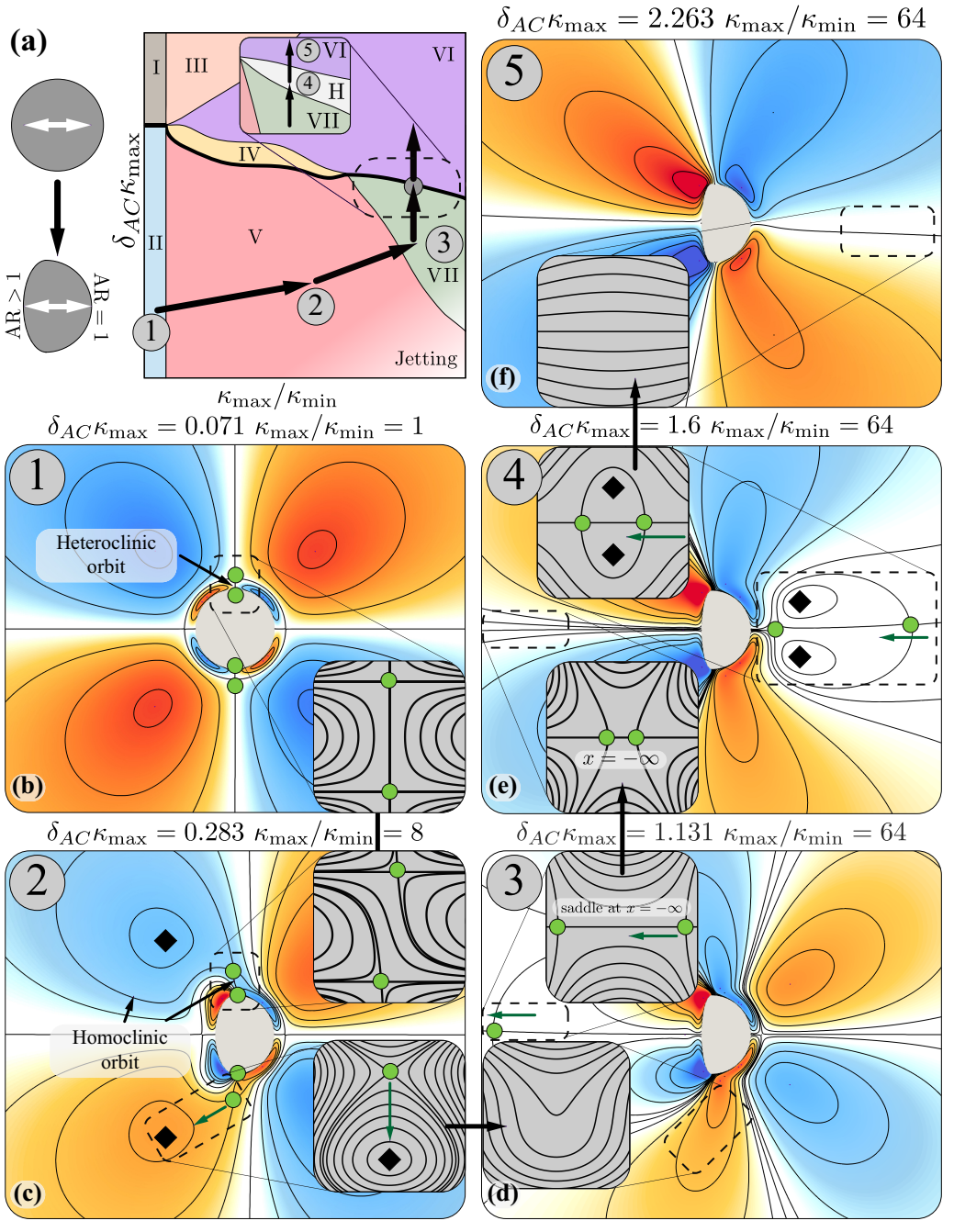

FIGURE 11. Flow topology manipulation. (*a*) Illustration of morphing a circular cylinder into a hybrid circular–elliptic cylinder. Mapping of the observed transitions on the lattice phase space. (*b-f*) present the different topologies observed on geometric and background flow variation, with the concerned critical points highlighted and the predictions (reduced Hamiltonian form contours) illustrated as grey contours.

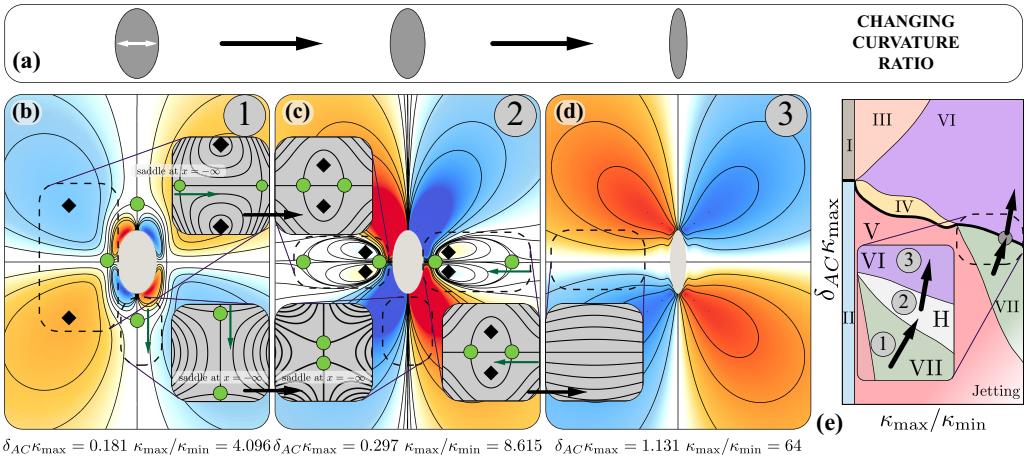

FIGURE 12. Flow topology manipulation. (a) Illustration of varying curvature of an ellipse by varying the aspect ratio AR. (b-d) present the different topologies observed on geometric variation, with the concerned critical points highlighted and the predictions (reduced Hamiltonian form contours) illustrated as grey contours. (e) Mapping of the observed transitions on the lattice phase space.

form closed recirculating regions on the left and right side of the ellipse. Computations of figure 12(c) confirm this intuition.

We then focus on the highlighted saddles and centres forming recirculating regions on the horizontal axis of the ellipse in figure 12(c). These structures closely resemble the hidden Phase H of figure 7(d, g). Based on our phase space, we predict that as $\delta_{AC}\kappa_{\max}$ increases (on increasing AR), the system will transition to a new topology corresponding to Phase VI, via a hyperbolic reflecting umbilic bifurcation. This is a consequence of the saddles and centres moving closer and closer, eventually collapsing and vanishing. Once again, computations of figure 12(d) confirm this intuition.

We note that in the ellipse case, due to its geometrical properties, some phases captured in our lattice phase space do not exist (see above discussion). Nonetheless, the phases and the transitions that do exist remain consistent with the lattice phase space, and so our analysis is still valid.

REFERENCES

BOSSCHAERT, MAIKEL & HANSSMANN, HEINZ 2013 Bifurcations in hamiltonian systems with a reflecting symmetry. *Qualitative Theory of Dynamical Systems* **12** (1), 67–87.

TATSUNO, MASAKAZU 1974 Circulatory streaming in the vicinity of an oscillating square cylinder. *Journal of the Physical Society of Japan* **36** (4), 1185–1191.

TATSUNO, MASAKAZU 1975 Circulatory streaming in the vicinity of an oscillating triangular cylinder. *Journal of the Physical Society of Japan* **38** (1), 257–264.